

## A Westward-Intensified Decadal Change in the North Pacific Thermocline and Gyre-Scale Circulation

ARTHUR J. MILLER, DANIEL R. CAYAN, AND WARREN B. WHITE

*Scripps Institution of Oceanography, La Jolla, California*

(Manuscript received 7 March 1996, in final form 12 January 1998)

### ABSTRACT

From the early 1970s to the mid-1980s, the main thermocline of the subarctic gyre of the North Pacific Ocean shoaled with temperatures at 200–400-m depth cooling by 1°–4°C over the region. The gyre-scale structure of the shoaling is quasi-stationary and intensified in the western part of the basin north of 30°N, suggesting concurrent changes in gyre-scale transport. A similar quasi-stationary cooling in the subtropical gyre south of 25°N is also observed but lags the subpolar change by several years. To explore the physics of these changes, the authors examine an ocean model forced by observed wind stress and heat flux anomalies from 1970–88 in which they find similar changes in gyre-scale thermocline structure. The model current fields reveal that the North Pacific subpolar and subtropical gyres strengthened by roughly 10% from the 1970s to the 1980s. The bulk of the eastward flow of the model Kuroshio–Oyashio Extension returned westward via the subpolar gyre circuit, while the subtropical gyre return flow along 20°N lags the subpolar changes by several years. The authors demonstrate that the model thermocline cooling and increased transport occurred in response to decadal-scale changes in basin-scale wind stress curl with the quasi-stationary oceanic response being in a time-dependent quasi-Sverdrup balance over much of the basin east of the date line. This wind stress curl driven response is quasi-stationary but occurs in conjunction with a propagating temperature anomaly associated with subduction in the central North Pacific that links the subpolar and subtropical gyre stationary changes and gives the appearance of circumgyre propagation. Different physics evidently controls the decadal subsurface temperature signal in different parts of the extratropical North Pacific.

### 1. Introduction

Changes in the ocean–atmosphere climate system with decadal timescales have been observed in a variety of variables. Particular interest has focused on climate change in the Pacific Ocean during the 1970s perhaps because of the large number of physical and biological variables involved (e.g., Ebbesmeyer et al. 1991; Graham 1994; Trenberth and Hurrell 1994; Miller et al. 1994a; Miller et al. 1994b).

In previous work, we have used observations and a model to diagnose the ocean dynamics and thermodynamics that prevailed in causing the surface layer of the ocean to shift from a warm sea surface temperature (SST) state in the central North Pacific to a cool SST state after the 1976–77 winter, and vice versa for the eastern North Pacific (Miller et al. 1994a; Miller et al. 1994b; Cayan et al. 1995). Anomalously strong horizontal advection teamed with surface heat flux forcing to install the new regime in the surface mixed layer.

Subsurface processes may have contributed to maintaining the surface mixed layer response in both regimes (Alexander and Deser 1995; Miller et al. 1994c).

In this study, we concentrate on the ocean beneath the mixed layer (in the main thermocline) in order to study a response that is insulated from direct turbulent and diabatic contact with the atmosphere. The reasoning is that mixed layer variables tend to bear spatial and temporal scales commensurate with the large-scale atmospheric forcing that predominantly drives them (Wallace et al. 1990; Cayan 1992; Miller et al. 1994a; Deser et al. 1996). In the thermocline, one instead anticipates that ocean dynamics will succeed in establishing the spatial structures and temporal variations that occur. To illustrate this point, Figs. 1a,c shows observed changes of the winter (January–March) SST and 400-m temperature from the early–mid-1970s to the early–mid-1980s (two 7-yr epochs motivated by results to be presented). The familiar canonical structure (e.g., Tanimoto et al. 1993) of cooling in the central North Pacific and warming along the eastern boundary seen in the SST is replaced at depth by a western-intensified structure in the temperature field north of 30°N that is reminiscent of gyre-scale circulation theory (e.g., Pedlosky 1987). This subsurface cooling in the Kuroshio Extension area

---

*Corresponding author address:* Arthur J. Miller, Climate Research Division, Scripps Institution of Oceanography, La Jolla, CA 92093-0224.  
E-mail: ajmiller@ucsd.edu

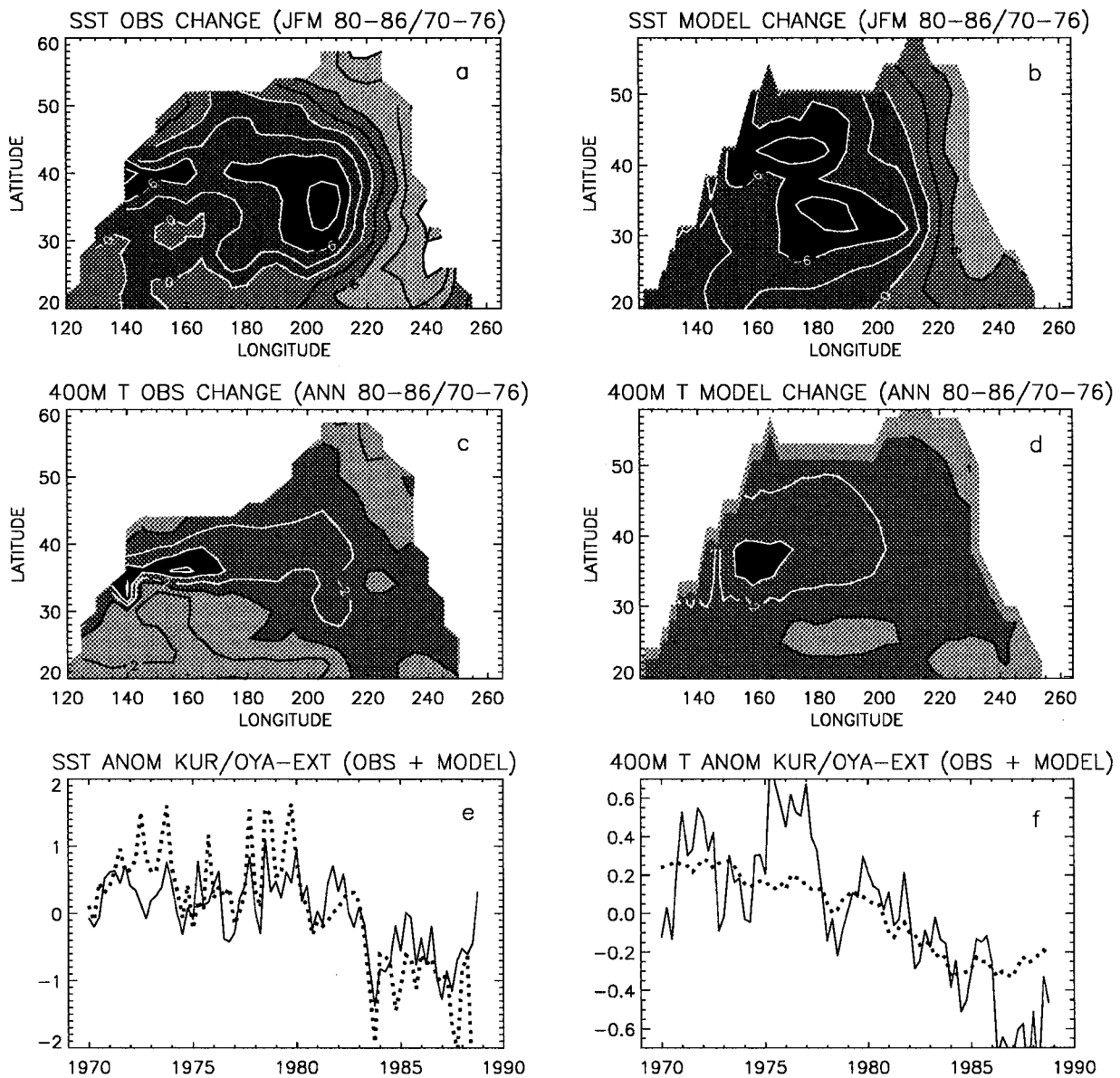


FIG. 1. Difference maps of the 7-yr periods 1980–86 relative to 1970–76 for (a) observed and (b) modeled winter (Jan–Mar) SST and (c) observed and (d) modeled annual 400-m temperature. Contour intervals (CI) are 0.3C for SST and 0.2C for 400 m with darker (lighter) shading negative (positive). Time series of observed (solid) and modeled (dotted) (e) SST and (f) 400 m averaged over the Kuroshio–Oyashio Extension region 35°–40°N, 150°E–180°. Correlation coefficients between model and observed are 0.71 in (e) and 0.78 in (f) due mainly to the decadal change signal.

was identified by Deser et al. (1996) and appears to extend up to the surface. We present evidence here that the previously observed local thermocline cooling is part of a basin-scale pattern of adjustment to wind stress curl forcing.

We here describe simple statistical analyses of observations of upper-ocean temperature for the period 1970–88 that reveal the decadal-scale change in North Pacific thermocline structure seen in Fig. 1c. A numerical hindcast of the ocean, forced by observed wind and

heat flux anomalies over the same time interval, reveals a similar change in upper-ocean thermocline structure (Fig. 1d) and provides additional information (unobtainable in the observations) of basin-scale velocity variations that are dynamically consistent with the forcing. Model analyses reveal that the decadal-scale thermocline change is forced by a basin-scale perturbation in wind stress curl that concomitantly strengthens the subpolar and subtropical gyres. This was provoked by a series of deepened Aleutian lows during winters of the

late 1970s and early 1980s that increased the westerly winds across midlatitudes and thereby increased the gyrescale wind stress curl (Ekman pumping).

We first describe the observational dataset (section 2) and model simulation (section 3), then explain the employed statistical analysis (section 4) of observed and modeled 400-m temperature fields that reveal the decadal-scale signal (section 5). Our results and related research are discussed and summarized in section 6. Some preliminary results of this work were reported by Miller (1996) and Miller et al. (1996).

## 2. Ocean temperature dataset

The temperature data consists of all available expendable current profiler (XBT), conductivity–temperature–depth probe/profiler, mechanical bathythermograph and standard hydrographic observations over the period 1955–92 assembled and quality controlled by the Scripps Joint Environmental Data Analysis Center. Processing of the raw hydrographic data to obtain anomalous temperatures at several standard depths from the surface to 400 m is described by White (1995). Since we wish to directly compare the data with a 1970–88 simulation we only use data from the 1970–88 time period, which is also the best-sampled time interval. A monthly mean climatology was computed for the period 1970–88, and monthly temperature anomalies were defined with respect to that climatology. Seasonal (winter being December–February, etc.) anomalies were then computed using those monthly mean temperature anomalies at a series of standard levels to 400-m depth on a  $2^\circ \text{ lat} \times 5^\circ \text{ long}$  grid. We wish to concentrate only on sub-mixed layer thermocline variations in this study so that mixed layer processes do not directly influence the response. The observed mixed layer in the open ocean, away from the western boundary, generally does not exceed 200 m (Suga and Hanawa 1990; Levitus 1982), so we considered only data from 250, 300, and 400 m. However, we found that all of the large-scale signals uncovered by our analysis are coherent between 250 and 400 m, with the variance decreasing with depth (resembling an equivalent barotropic response). Therefore our discussion and analysis here will rely solely on the data at 400 m, which is less likely to be directly influenced by surface mixed layer processes than shallower levels.

Figure 2a shows the rms-observed temperature variations of seasonal anomalies at 400-m depth north of  $10^\circ\text{N}$  in the North Pacific over the time interval of interest. The rms values are based on all seasons within the study period, where seasons are defined as the 3-month average of December, January, and February, etc. Typical observed anomalies are roughly  $0.6^\circ\text{C}$  in the open ocean. White (1995) estimates standard error bars on 400-m temperature anomalies to be  $\pm 0.2^\circ\text{C}$  for 2-yr timescales, so they will be slightly larger for these seasonal anomalies. Two pronounced maxima occur where

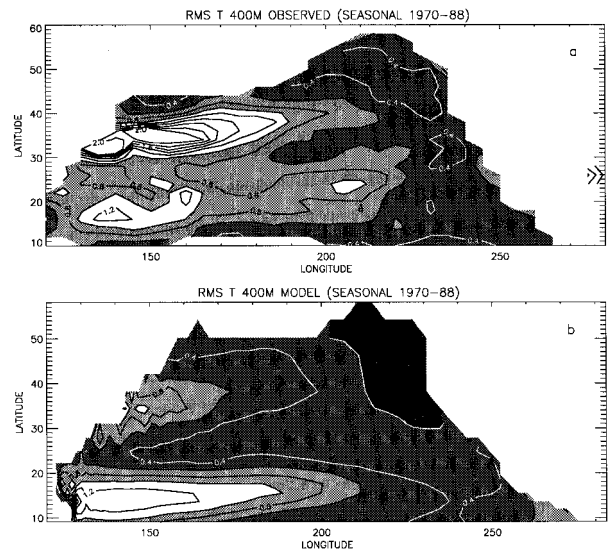


FIG. 2. Rms temperature variations at 400-m depth for seasonal anomalies over the period 1970–88 for (a) observations and (b) model. Regions of insufficient data in (a) or land in (b) are left white. The CI is  $0.2^\circ$ , with lower values shaded darker and higher values shaded lighter.

the rms temperature is much higher, one in the Kuroshio–Oyashio Extension region near  $35^\circ\text{N}$  and the other in the return flow region of the subtropical gyre near  $20^\circ\text{N}$ . A weaker maximum occurs in the central North Pacific near  $20^\circ\text{N}$ – $160^\circ\text{W}$ , associated with subducted temperature anomalies (Deser et al. 1996; Schneider et al. 1999). This map gives us a general picture of the patterns and amplitude of 400-m temperature variability across the North Pacific.

## 3. 1970–88 ocean model simulation

The primitive equation ocean model was developed by Oberhuber (1993) and applied by Miller et al. (1994a) to study monthly mean through decadal-scale variations over the Pacific basin ( $60^\circ\text{N}$ – $76^\circ\text{S}$ ). The model is constructed from eight isopycnal layers (each with constant potential density but variable thickness, temperature, and salinity) fully coupled to a bulk surface mixed layer model. The resolution is relatively coarse ( $4^\circ$  in open ocean but with finer resolution near the equator and eastern–western boundaries) so only large-scale patterns can be considered with confidence. The surface forcing consists of a climatological monthly mean seasonal cycle of wind stress, total surface heat flux, and turbulent kinetic energy input to the mixed layer, to which are respectively added the specified observed monthly mean anomalies (linearly interpolated from month to month) derived from The Comprehensive Ocean–Atmosphere Data Set observations for the period 1965–88. In the  $20^\circ\text{N}$ – $20^\circ\text{S}$  latitude band, heat fluxes are parameterized as a Newtonian cooling to the model SST monthly mean climatology (computed from the

spinup period). There is no ocean feedback to the anomalous forcing so that the model is not constrained to reproduce the observed temperature variations. Anomalous freshwater fluxes are not included here; surface mixed layer salinity is damped (Newtonian relaxation constant =  $5 \times 10^{-6} \text{ m s}^{-1}$ ) to the Levitus annual mean salinity field.

A thorough discussion of the model framework and forcing technique is provided by Miller et al. (1994a). A basic tenet of this modeling strategy is that the variability to be captured is driven by atmospheric forcing. This point is especially subtle with regard to using heat flux anomalies specified from observations as part of the surface forcing. These heat flux anomalies are here presumed to be driving the SST anomalies (cf. Cayan 1992) even on long timescales when ocean feedback to the atmosphere may occur in nature. If this feedback effect is strong enough, then the modeling assumption will likely break down and model SST will poorly match observations since the fluxes would drive model anomalies even though in nature they would be damping them. As long as the specified heat flux anomalies tend to zero at lowest frequencies (Barsugli and Battisti 1998), this problem should be minimized. The model's response to wind stress forcing anomalies should be more robust, although coarse resolution can severely limit the model's ability to properly model advective effects of currents and waves on surface and subsurface temperature anomalies. If coupled modes of midlatitude Pacific decadal variability are occurring in nature (such as suggested by the modeling results of Latif and Barnett 1994 and Robertson 1996), the oceanic portion of that coupled phenomenon could appear here as a disguised forced response. Fully coupled simulations, as opposed to hindcast case studies described here, are needed to untangle that web of interaction.

Since decadal variations may be either abrupt or gradual, it is important to include the higher-frequency forcing to distinguish which aspects of the modeled response are a consequence of the specified forcing or of the oceanic dynamics and thermodynamics. For example, the mixed layer SST shift in 1976–77 is rather steplike (Miller et al. 1994a,b), so that a low-passed input forcing would not have cleanly captured this event. The decadal thermocline change studied here is much more gradual, however, so that low-passed forcing is likely sufficient. Only the model output from 1970 through 1988 (specifically, December 1969 through November 1988) is considered here; this allows a 5-yr equilibration period (1965–69) for the anomalous response. Additional analyses and verifications of the simulation are discussed by Cayan et al. (1995) and Miller et al. (1994a,b; Miller et al. 1994c)

Surface mixed layer variables were saved as monthly mean quantities, but subsurface isopycnal layer fields were stored only once per month (on day 15 of each 30-day month). Even though monthly mean forcing fields were used, the model generates weak variability

on shorter timescales for a variety of reasons so that the monthly sampling interval will result in aliasing of these weak shorter timescale motions. We compared the monthly mean surface velocity fields with those day 15 monthly sampling fields and found that differences are usually less than 10% of the true monthly mean fields. In our analysis of seasonal averages, we will have an even lower error for these estimates of the true model monthly mean fields at depth; for the decadal timescale change to be identified the sampling problem should be inconsequential.

Model climatologies for all the variables of interest (e.g., temperature and horizontal velocity at various depths, isopycnal-layer depth variations, input wind stress curl) were computed for the 1970–88 interval and anomalies discussed below are relative to this monthly mean seasonal cycle state. Note that the model mixed layer never exceeded 250-m depth in the open ocean North Pacific, so we can concentrate on anomalies at 250 m and greater when isolating ocean dynamics from mixed layer physics. As found in the observations, 400-m anomalies are coherent with and weaker than the sub-mixed layer anomalies at shallower depths so that they resemble an equivalent barotropic flow.

Figure 1e shows time variations of the model and observed winter SST in a rectangular region of the Kuroshio–Oyashio Extension ( $35^{\circ}\text{N}$ – $40^{\circ}\text{N}$ ;  $150^{\circ}\text{E}$ – $180^{\circ}\text{W}$ ). Winter SST is shown rather than annual because SST during the deep mixed layer season is more persistent and representative of annual conditions than is SST during the thin summer mixed layer season. The model variations are fairly well matched to the observed winter SST anomalies (anomaly correlation coefficient = 0.71), although the model anomalies are somewhat larger in amplitude. At 400-m depth in the same area (Fig. 1f), the model adequately predicts the amplitude of the decadal temperature variation but clearly does not capture the shorter period interannual variations. These latter fluctuations may be due to local eddy dynamics or other air–sea interaction phenomena not included in this hindcast scenario (e.g., Yamagata and Masumoto 1992; Jiang et al. 1995; Spall 1996). The correlation coefficient between model and observed 400-m temperature is still high (0.78), however, because of the presence of the the decadal trend that allows the short-period fluctuations to be averaged out.

Figure 2b shows the model rms 400-m temperature distribution for comparison with the observed (top). The typical model temperature variation at 400 m has an amplitude roughly half that of the observations. This is partly due to using monthly mean observations as the forcing functions, rather than the synoptically (and diurnally) varying true input forcing, and the concomitant underestimation of wind stress curl over long timescales. It also may be partly due to a mean vertical temperature gradient which is weaker than observed. Lastly, the method we used to input the monthly mean wind stress and heat flux anomalies (linear interpolation



between the 15th of each month) inadvertently results in 30-day averaged forcing anomalies that are weaker than observed (Killworth 1996). The model does capture the dual maximum in rms temperature, though it underestimates the strength of the Kuroshio–Oyashio Extension peak and overestimates the subtropical gyre return flow peak. The former is likely due to the lack of eddy-resolving physics in the model, while the latter may be due to undersampling in the data. Nonetheless, the basic model character seen in Figs. 1 and 2 is sufficiently realistic to proceed with a detailed comparison of model and observations on the decadal timescale.

#### 4. Extended EOF analysis

An advantage of considering the sub-mixed layer temperature is that this layer provides a view of the upper-ocean dynamic response that is uncontaminated by direct turbulent surface forcing. Thus, if dynamically propagating features are present, they might be more clearly distinguished from signals driven by propagating atmospheric surface forcing. In order to best isolate any propagating features of the thermocline anomalies, we used an extended empirical orthogonal function (EEOF) analysis. In this dataset, this procedure is superior to standard EOF analysis in that it aids in cleanly separating the two dominant timescales that occur in the analyses (decadal and interannual), only one of which exhibits significant propagating features; standard EOFs tend to mix the two timescales and confuse the interpretation of response. The EEOF technique has frequently been used in oceanographic and atmospheric problems to identify dominant patterns of space–time relationships (e.g., Weare and Nasstrom 1982; Robertson et al. 1995), specifically cyclical behavior in the field. It is essentially the same as multichannel singular spectrum analysis (Vautard and Ghil 1989). The covariance matrix is constructed with the original time series supplemented with time-lagged versions of the original time series. As the number of lags increases, the time series must be shortened so there is a trade-off between maximizing the degrees of freedom yet allowing the lags to span the interval of the oscillating feature. An excellent discussion of EEOFs is given by von Storch and Frankignoul (1996) in the context of many other techniques of statistical modal decomposition.

Seasonal anomalies were constructed for all observed and modeled fields on a subgrid that spanned approximately 20°–60°N and 160°E to the eastern boundary. This domain was chosen to 1) isolate the midlatitudes from the energetic variations with ENSO timescales that occur in the tropical strip, 2) exclude the poorly sampled (in observations) and poorly modeled variations near the western boundary currents, and 3) exclude the relatively coarsely sampled low latitudes south of 20°N. The time interval of 1970–88 was selected because 1) observations before 1970 are more poorly sampled and 2) the model simulation corresponds to that time interval

allowing for direct comparison to observations. In the EEOFs, the seasonal anomalies were extended by including seasonally lagged fields out to 3 yr (13 total lags) from which the eigensolutions of the covariance matrix were computed. This choice of lags allows us to distinguish propagating features in timescales as long as 3 yr. Lower-frequency timescales (including trends or fluctuations with periods longer than roughly 3 yr) are consequently lumped together, and propagation can only be distinguished over a fraction of the low-frequency period.

We also computed the combined EEOFs (e.g., Bretherton et al. 1992) of several pairs of variables to identify common patterns between the two fields. In combined EEOFs, more than one type of field is included in the time series from which the covariance matrix is constructed. The results link spatial patterns in each type of field to the time variability of a principal component; the spatial patterns of the fields for each EOF need not be similar. If the fields are not the same unit (e.g., velocity and temperature), each field is here normalized by a single number, the rms value of the field computed over the entire domain. EEOFs were computed for 1) XBT observations of 400-m temperature alone, 2) XBT observations and modeled 400-m temperature together, 3) model temperature and model velocity together, and 4) the important terms in the vertically integrated vorticity equation.

Questions regarding statistical significance of results necessarily arise with any statistical technique. Assumptions concerning noise in the system (the observed XBT dataset, the observed atmospheric model forcing, etc.) could be made to develop reliability statistics. However, since we are studying essentially one realization of a decadal event here, the results must be considered as a case study. In many respects, the decadal signal represents a trendlike low-pass filtered version of the data with the high-frequency variability excised by the EEOF technique. The following discussion pertains essentially to only the highest (or one of the highest) EEOF eigenvalues of the system that describe a relatively high amount of the variance and are well separated from the red noise background, so we used an ad hoc method to estimate degrees of freedom in placing error bars on the eigenvalues. Moreover, the statistical results are substantiated by physical interpretation, which is a key point of validation.

More sophisticated model testing strategies have been designed by, for example, Schröter and Wunsch (1986) and Frankignoul et al. (1989), in which the sensitivity of an ocean model to changes in forcing are computed in ensembles of runs of the model. The results provide quantitative limits on how well a model performs with respect to reproducing data, but the computational requirements can be ominous for large ocean models and the results are dependent on the specified error covariance of the forcing functions and the validating data. We will consider only simple quantitative measures,

such as pattern correlations, for model validation in the following discussion.

## 5. Results

Two dominant timescales emerge from our various oceanic EEOF analyses. The primary signal, which explains roughly one-quarter of the variance, has a decadal timescale and is the subject of this presentation. The second most important signal is a propagating pair of EEOFs, which together explain roughly 10% of the variance and that bear interannual timescales; this pair of modes is discussed in a separate publication (Miller et al. 1997). We now describe the spatial patterns and temporal variations of this decadal signal.

### a. Observed 400-m temperature alone

We first consider 400-m temperature in the observations alone. Figure 3 shows the EEOFs (subsamped for lags 0, 1.5, and 3 yr) for the first two modes that describe 23% and 8% of the variance, respectively. Using an ad hoc estimate of the degrees of freedom of the dataset based on a 1-yr integral timescale (e.g., North et al. 1982) yields error bars of  $\pm 0.32$  times the eigenvalues (68% confidence intervals). Error bars are half that range for the spectrum of high-frequency noise. The first and second eigenvalues are thus well separated from the noise background of the eigenvalue spectrum, which is red and drops well below unity for modes numbered greater than 25 (Fig. 3h).

The first EEOF (Fig. 3, left) is dominated by a stationary pattern between  $30^\circ$  and  $45^\circ\text{N}$ , that increases in amplitude toward the western part of the analysis domain ( $160^\circ\text{E}$ ). This pattern is largely associated with the spatial location of the Kuroshio–Oyashio Extension and the southern flanks of the subpolar gyre. The EEOF also reveals a nearly stationary signal that grows in time, spreads westward, and is centered around  $140^\circ$ – $160^\circ\text{W}$  and  $25^\circ\text{N}$ . The time variation of this pattern is shown in Fig. 3g where it can be seen that it has a decadal-scale scale. Commencing in the early 1970s, it represents an anomalously warm thermocline (temperature at 400 m) in the northwestern Pacific and reverses sign circa 1979 as it enters a cool regime.

The second EEOF (Fig. 3, right) explains much less variance than does EEOF-1 but it also exhibits a decadal timescale that changes sign in the mid-1970s and early 1980s, with an apparent out of phase relationship with the dominant first EEOF (Fig. 3g). The spatial pattern of the second mode, which tends to be concentrated in the eastern and central North Pacific, is also nearly stationary but grows and spreads northwestward in time.

Although the time variations of these two modes appear to be  $90^\circ$  out of phase (assuming a 20-yr period), the mismatch in spatial patterns and the disparity of explained variances suggest that they do not represent a prominent propagating wavelike feature (cf. Zhang

and Levitus 1997). Instead they represent a dominant stationary feature (the western intensified hump near  $38^\circ\text{N}$ ) which flips sign from the early 1970s to the early 1980s. Concurrent with this is weaker growth/decay of spreading features separate from the hump. We will later present evidence that the dominant westward-intensified stationary feature is driven by wind-stress curl forcing, while the much weaker propagating component is associated with anomalous subduction (Deser et al. 1996; Schneider et al. 1999).

### b. Observed and modeled 400-m temperature

We next seek to identify how well the model is able to capture aspects of the observations described in section 5a. We first computed EEOFs of model 400-m temperature alone and found a similar dominance of a westward-intensified stationary decadal cooling in the subpolar gyre. For brevity, this EEOF is not shown since this pattern and time variation are evident in the other EEOFs to be discussed later. In order to extract the model and observed spatial patterns that vary in time together, we combined the model and observed fields before computing the EEOFs. Since the model temperature variations are somewhat weaker than those observed, we normalized the time series with the rms value of the fields averaged over the entire analysis subdomain ( $\text{rms } T_m = 0.13^\circ\text{C}$ ,  $\text{rms } T_o = 0.25^\circ\text{C}$ ).

The first combined EEOF of 400-m temperature explains 29% of the combined variance and is shown in Fig. 4. It is well separated from the red spectrum of eigenvalues. The time variation (Fig. 4g) is decidedly decadal and also compares well with that of the observations alone (Fig. 3g). Comparison with Fig. 3 reveals that the observed portion is essentially the same pattern as the first EEOF of the observations alone. The pattern correlation between the observed and modeled 400-m temperature is 0.64 for zero lag, reaches a maximum of 0.71 for the 1-yr lagged fields, and gradually drops to a minimum of 0.58 for 3-yr lagged fields. The model pattern has a western intensified hump between  $35^\circ$  and  $45^\circ\text{N}$ , which is similar to the observed pattern although the model hump has greater north–south extent compared to the data (which has poor coverage north of  $45^\circ\text{N}$ ). The model pattern also fails to capture the growing and spreading (subducting) feature near  $160^\circ\text{W}$  and  $25^\circ\text{N}$  in the observed 400-m temperature. Last, the model pattern has an additional signal south of  $22^\circ\text{N}$  that grows in time with respect to the stationary high-latitude feature and does not appear to directly correspond to any feature in the observations. It appears to be associated with a response of the subtropical gyre thermocline, lagged in time by several years with respect to the subpolar thermocline response, as found in XBT analyses by Zhang and Levitus (1997) and Tourre et al. (1999). A larger analysis domain in our study captures that subtropical gyre thermocline response in the observations.

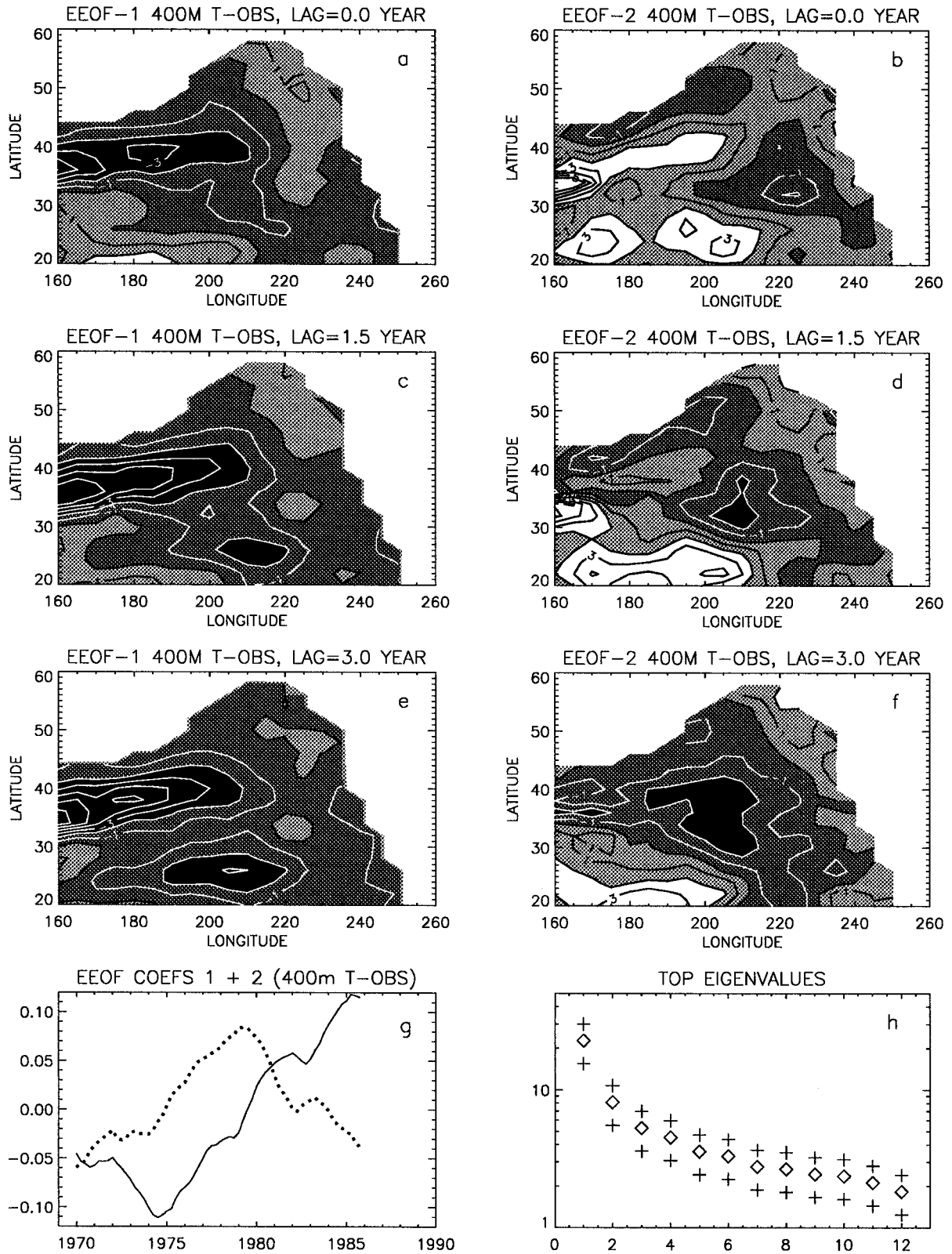


FIG. 3. (Left panels) Maps of EEOF-1 of seasonal anomalies of observed 400-m temperature in the North Pacific for (a) 0-yr, (c) 1.5-yr, and (e) 3-yr lags (complete lags include 0 through 12 seasons). (Right panels) Same for EEOF-2 for (b) 0-yr, (d) 1.5-yr, and (f) 3-yr lags. The CI is 1°C, with darker shading negative and lighter positive. (g) Time series of the principal components of EEOF-1 (solid, 23% of total variance) and EEOF-2 (dashed, 8%). (h) Eigenvalue spectrum (diamonds) with 68% confidence intervals (pluses) based on 1-yr interannual decorrelation time.



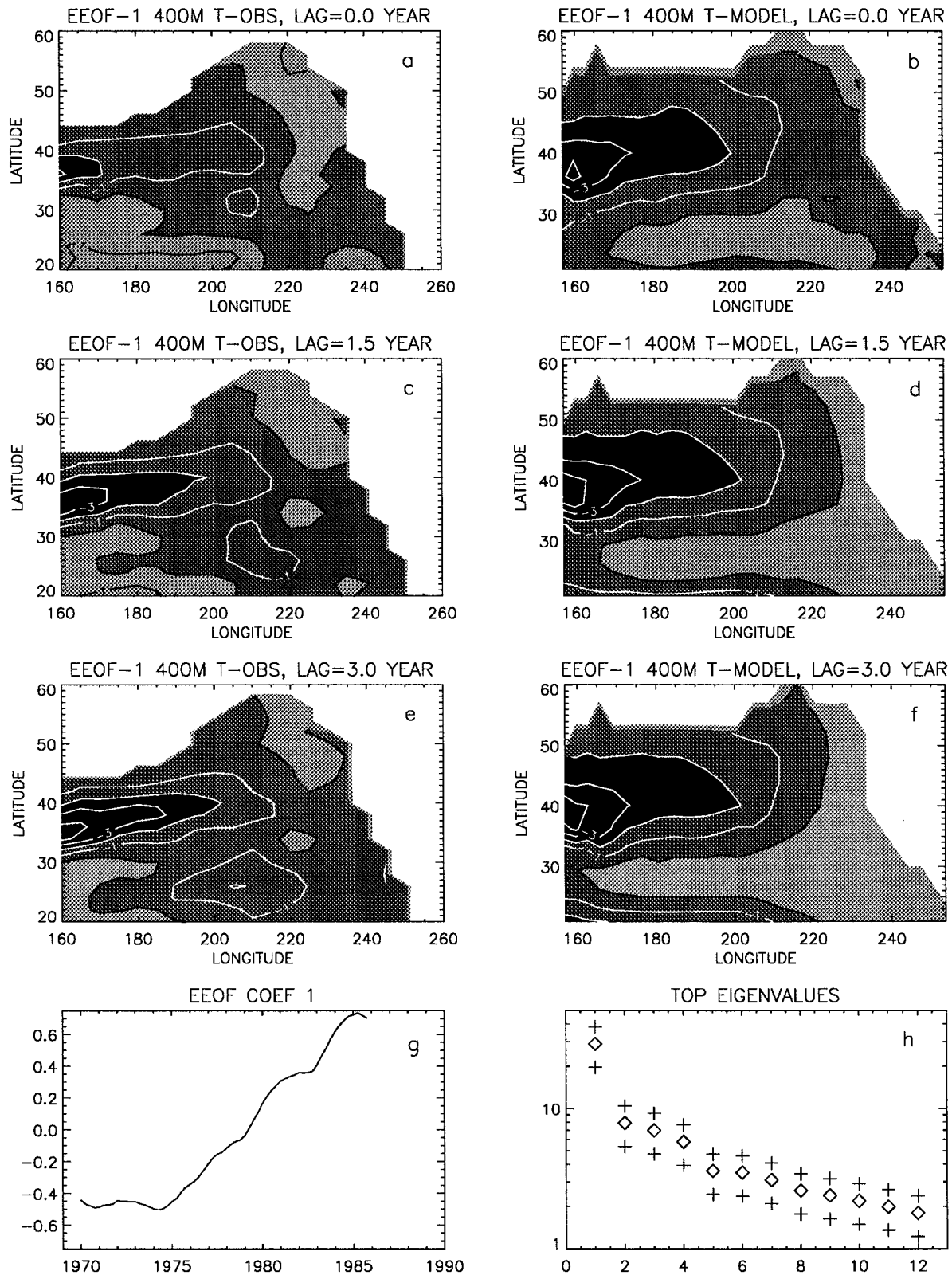


FIG. 4. Maps of combined EEOF-1 of seasonal anomalies of observed 400-m temperature [(a), (c), (e): normalized by 0.25°C] and model 400-m temperature [(b), (d), (f): normalized by 0.13°C] in the North Pacific for (top panel) 0-yr, (middle panel) 1.5-yr, and (lower panel) 3-yr lags (complete lags include 0 through 12 seasons). The CI is 1°C, with darker values negative and lighter values positive. The pattern correlations between observed and modeled fields are 0.64, 0.70, and 0.58 for 0-yr, 1.5-yr, and 3-yr lags, respectively. (g) Time series of the principal component (29% of total variance). (h) Eigenvalue spectrum (diamonds) with 68% confidence intervals (pluses) based on 1-yr interannual decorrelation time.



There is no combined mode in this case, or the case with model 400-m temperature alone, that captures the subordinate (subducting) feature near 25°N, 160°W. We will speculate in the discussion in later sections as to why this feature (apparently forced by differing physics than the rest of the temperature field) does not occur in the simulation.

We have found that the model captures the dominant stationary feature observed in the 400-m temperature data: a western intensified decadal-scale cooling of the thermocline (400-m temperature) between 30° and 50°N. Since this feature is the dominant signal, we seek to explain its dynamics by analyzing the model version of this signal in more detail in the following sections.

### c. Model temperature and velocity

We next examine the model's 400-m temperature and velocity field together in combined EEOFs. The model velocity field can be studied over the basin scale in a way unobtainable from present observations. Furthermore, the model velocity field is dynamically consistent with the model temperature field unlike estimates of observed temperature and velocity that are obscured by noise. The model temperature and velocity vectors are each normalized by their rms values averaged over the analysis domain, respectively,  $T_m = 0.13^\circ$  and  $|\mathbf{u}| = 0.35 \text{ cm s}^{-1}$ . The first EEOF explains 21% of the combined variance and again corresponds to the decadal signal previously identified. Since this is nearly a stationary pattern over the 3 yr of seasonal lags, we only plot the average of the 13 EEOF lags in Figs. 5a,c. (Note that this EEOF averaging process is superior to computing standard EOFs because they result in the dominant decadal mode being contaminated by propagating interannual variations.)

Figures 5a,c show the first combined EEOF in which one can see the velocity field associated with the changes in the thermocline. Generally, the velocity field shows that 400-m currents follow the 400-m temperature contours in the sense of geostrophic flow. The spatial structure of the velocity pattern is fairly well matched to the spatial structure of the mean gyre-scale circulation in the model. Thus by examining the time series of the EEOF coefficient (Fig. 5e) we can see that the Kuroshio–Oyashio Extension (along 35°N), the subtropical gyre return flow (along 45°–50°N) and the sub-

tropical gyre return flow (along 20°N) were all strengthened from the early–mid-1970s to the early–mid-1980s. The subtropical gyre return flow appears to lag the development of the subpolar gyre by several years in the EEOF analysis, an observation identified by Tourre et al. (1999) and Zhang and Levitus (1996). Also an anomalously northward flow into the central part of the Gulf of Alaska developed in the model over this time interval. Little change in velocity occurs along the west coast of North America in the California Current at this depth as discussed in more detail by Miller (1996).

### d. Observed wind stress curl and model transport

A candidate mechanism for driving the modeled decadal change in gyre-scale circulation is the increase in wind stress that was observed to occur in association with the strengthened Aleutian lows during winter over the North Pacific in the mid-1970s. In the surface layer, both Ekman currents and geostrophic currents contribute to the total modeled current field. Indeed combined EOFs (not shown) of wind stress and model surface (mixed layer) currents reveal patterns consistent with an Ekman response on monthly timescales. Since we are considering the temperature and velocity patterns at 400-m depth, well beneath the mixed layer, we expect that these nearly geostrophic currents will be more likely related to wind stress curl variations and the associated Ekman pumping.

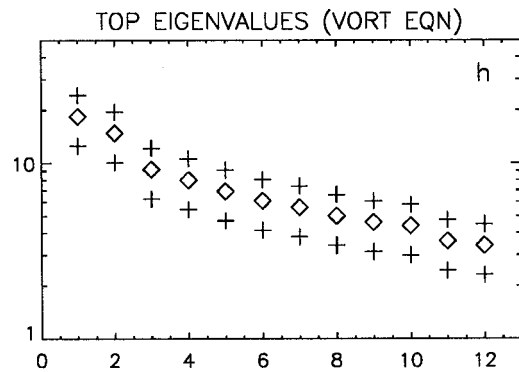
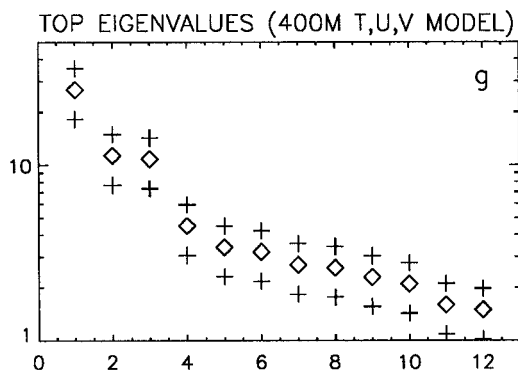
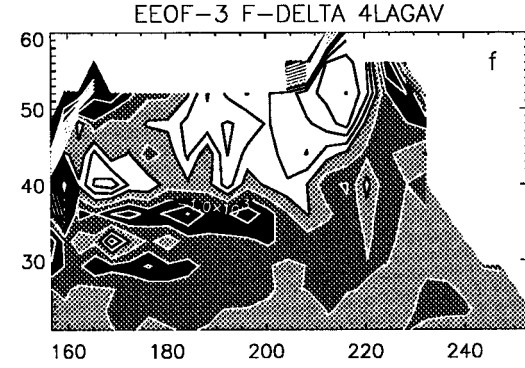
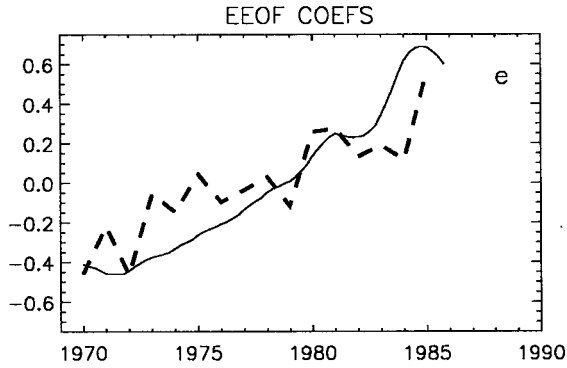
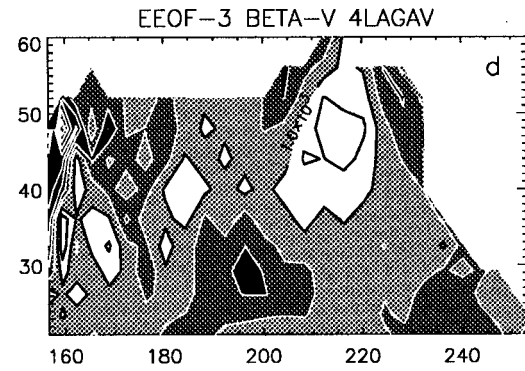
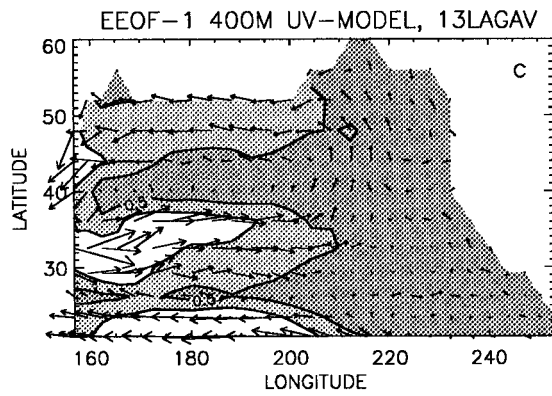
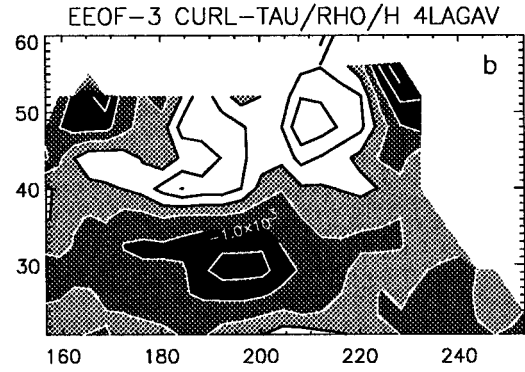
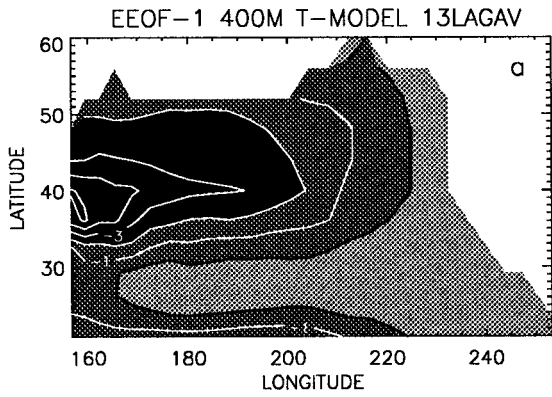
We therefore test the hypothesis that anomalous wind stress curl drives the anomalous model decadal temperature and velocity patterns by studying the vertically integrated (from 0 to 1500 m) vorticity equation,

$$\zeta_t + \beta v + f\delta = \frac{\text{curl}\tau}{\rho H} + D, \quad (1)$$

where  $\zeta$  is the vertically integrated vorticity,  $\delta$  is the vertically integrated horizontal divergence,  $v$  is the vertically integrated meridional velocity,  $\tau$  is the wind stress (derived from observations),  $D$  is damping,  $f$  is the latitudinally dependent Coriolis parameter, and  $\beta$  is its latitudinally dependent meridional derivative.

The relative vorticity term in (1) is at least a factor or 10 smaller than the other terms on these timescales, and damping is sufficiently small to be disregarded. We therefore seek large-scale relations among the three dominant terms in (1), the divergence term (proportional

FIG. 5. (a), (c) Synopsis of combined EEOF-1 of seasonal anomalies of modeled 400-m temperature [(a): normalized by 0.2°C] and modeled 400-m velocity [(c): normalized by 0.05 cm s<sup>-1</sup>] in the North Pacific, plotted as an average of all 13 lags (0 through 12 seasons) for brevity. The CI is 1.0 for temperature and 0.5 for velocity, with darker values smaller and lighter values larger. (b), (d), (f): Synopsis of combined EEOF-3 of annual anomalies of the three dominant terms of the vertically integrated (0–1500 m) vorticity Eq. (2), (b) curl  $\tau$  term, (d) north–south transport term, and (f) divergence term in the reduced-domain North Pacific, plotted as an average of all 13 lags (0 through 12 seasons) for brevity. The CI is  $1 \times 10^3 \text{ s}^{-2}$ , with black and dark-gray shading negative and light-gray and white shading positive. (e) Time series of the principal component of (solid) EEOF-1 above (27% of total variance) and (dashed) EEOF-3 above (9% of total variance). Eigenvalue spectra (diamonds) of (g) 400-m temperature and velocity and (h) vorticity equation, with 68% confidence intervals (plusses) based on 1-yr interannual decorrelation time.



to deflection of the lower interface by the continuity equation, that is, vortex stretching), the beta term, and the Ekman pumping term,

$$\beta v + f\delta \approx \frac{\text{curl}\tau}{\rho H}. \quad (2)$$

Equation (1) was evaluated as local balance at each grid point. Because complete model fields were archived only once per month, the terms in (1) must be reconstructed and an exact balance of terms each month is not achievable. The results of the following statistical analysis (the terms of which also are not exactly balanced), however, suggest that the large-scale patterns of variability among the terms can nonetheless be identified.

To suppress higher-frequency wind stress curl variations and possible aliasing due to the monthly archiving, we computed annual anomalies in a three-term combined EOF (4-yr-long lags from 0 to 3 yr) of (2). Annual averages (with lags out to 3 yr) were used because the high-frequency variability of the input wind stress fluctuations causes the decadal signal to be immersed in the middling EOF modes of seasonal averages. Even with annual anomalies, the first two combined EOFs of (2) (explaining 33% of the annual anomaly combined variance) correspond to interannual, ENSO-scale variations (Miller et al. 1997). The third EOF describes 9% of the combined annual anomaly variance and corresponds to the decadal change as can be seen by the time variability and the spatial patterns (Fig. 5, right). This mode is not as well separated from the red background (Fig. 5h) as in previous cases but lies above the noise of much higher mode numbers and also has a clear physical explanation.

The patterns of the third EOF are shown in Figs. 5b,d,f, plotted as an average over the four annual lags for brevity, since the response is stationary. This figure reveals that a large-scale pattern of wind stress curl (Fig. 5b) is associated dynamically with the pattern of north-south transport (Fig. 5d) corresponding to the decadal velocity (Fig. 5c) and temperature (Fig. 5a) change in the subpolar gyre east of the date line. West of about 180°, the statistical analysis of the dynamics yields a noisy result, suggesting grid-scale Rossby waves are prevalent in the model velocity field.

If anomalous wind stress curl and north-south transport balanced exactly, a Sverdrup balance would hold (Trenberth 1991). Instead we find that the vertical velocity at the base of the 1500-m vertically integrated layer is significantly nonzero. This suggests that either the gyre-scale currents have not equilibrated or that bottom topography is interfering with the Sverdrup balance. Because the lowest model isopycnal layer is very thick (typically 3500 m) the vertical velocity at 1500 m is certainly influenced by the variable topography in the North Pacific resulting in nonnegligible vertical velocity fields at the top of that lowest layer. It appears that this

baroclinic topographic effect defeats the quantitative Sverdrup balance. Nonetheless the similarity in spatial patterns and time variations between the wind stress curl and the north-south transport supports the idea that the surface fields are driven by the decadal-scale wind stress curl change.

Thus, a quasi-Sverdrup balance appears to have been attained east of roughly 180° based on this statistical analysis of local balances. Typical estimation of Sverdrup balance in the ocean is done by horizontally integrating the flow westward from the eastern boundary in order to suppress high wavenumber variations (e.g., Hautala et al. 1994). Indeed, we computed combined EOFs of 400-m temperature and wind stress curl (not shown) and found the same western intensified patterns of 400-m temperature seen in Figs. 4 and 5a and the same wind stress curl pattern seen in Fig. 5b. As derived by Anderson and Gill (1975), long Rossby waves emanating from the eastern boundary slowly propagate westward and gradually equilibrate the midlatitude gyre response to changing wind systems. Typical values for the (nondispersive) group velocity in the latitude band 30°–45°N range from 0.8 to 1.8 cm s<sup>-1</sup> (Emery et al. 1984). Thus, the characteristic time required to transmit information from the eastern boundary 5000 km westward to the date line would be 8–18 yr based on linear wave dynamics. Recent satellite and in situ observations of Rossby wave propagation suggest phase speeds are larger than the theoretical speed (Chelton and Schlax 1996; Miller et al. 1997; but cf. Sturges and Hong 1995). Thus the modeled eastern basin adjustment pattern is consistent with a relatively fast phase speed of Rossby wave propagation. And although the western North Pacific basin has not equilibrated into a Sverdrup (or topographic-Sverdrup) balance, the thermocline in that region adjusts locally by other effects (e.g., local Ekman pumping, eastward propagating Rossby waves, etc.) in a pattern consistent with a quasi-Sverdrup balance.

The wind stress curl increase from the early-mid-1970s to the early-mid-1980s (plotted in Fig. 6a as a difference of two 7-yr epochs motivated by the EOF analyses) is thus associated with a gyre-scale circulation change. Simple gyre-scale circulation theory can be invoked to predict the change in geostrophic streamfunction driven by the Ekman pumping associated with the wind stress curl change. If we assume that an equivalent barotropic layer (of roughly 400-m depth) rests atop a motionless lower layer representing the remainder of the water column, the steady-state upper-layer geostrophic streamfunction can be found according to (Pedlosky 1987)

$$\beta\psi_x = \frac{f}{\rho_0 H} \text{curl}\left(\frac{\tau}{f}\right). \quad (3)$$

Figure 6b shows the result of integrating (3) westward across the basin from the the eastern boundary (where we have arbitrarily defined  $\psi = 0$  although eastern



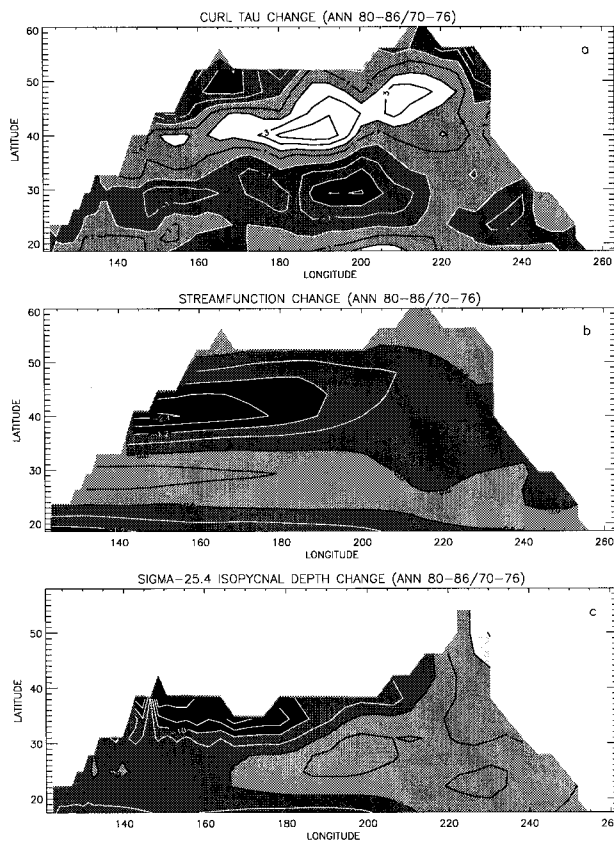


FIG. 6. (a) Observed wind stress curl forcing change based on the difference of the period 1980–86 relative to 1970–76. The CI is  $1 \text{ N m}^{-3}$ , scaled by  $10^7$ . (Middle panel) Theoretical streamfunction solution to Eq. (3) as a response to the Ekman pumping velocity, curl ( $\tau/f$ ), implied by the wind stress curl change above. CI of  $1 \text{ m}^2 \text{ s}^{-1}$ , scaled by  $10^7$ . (Bottom panel) Model depth change of the  $\sigma_\theta = 25.4$  layer based on the difference of the period 1980–86 relative to 1970–76. The mean distribution of this layer varies from 80–160 m near the eastern boundary to 200–280 m near the Kuroshio–Oyashio Extension region. During winter the model  $\sigma_\theta$  isopycnal layer intersects the mixed layer along  $40^\circ\text{N}$  and into the Gulf of Alaska, so the change is not plotted wherever it intersects the surface. The CI is 5 m with darker values shallower and lighter values deeper.

boundary layers may require otherwise) assuming  $H = 400 \text{ m}$  and  $\beta$  and  $f$  are latitudinally dependent. The circulation changes seen in the model (Figs. 5c,d and Fig. 7) correspond to the strongest gradients evident in Fig. 6b. Since the streamfunction in this simple model is also proportional to the interface deflection,  $\eta = f\psi/g'$ , where  $g'$  is a reduced gravity, the pattern seen in Fig. 6b is also proportional to the temperature change at the interface which is evidently similar to that of the model and observations (Figs. 1, 3, 4, and 5). As previously mentioned, a combined EEOF (not shown) using 400-m temperature and wind stress curl yields essentially the same patterns of temperature seen in Figs. 4 and 5 and of wind stress curl (Ekman pumping velocity) seen in Figs. 5 and 6.

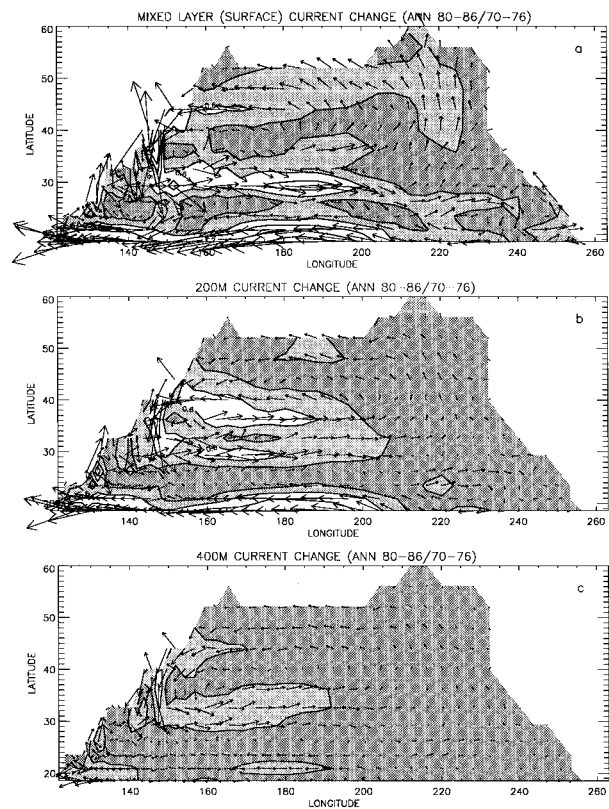


FIG. 7. Maps of model (a) surface layer, (b) 200- and (c) 400-m current change based on the difference of the period 1980–86 relative to 1970–76. Current speed plotted with CI of  $0.3 \text{ cm s}^{-1}$  with darker values smaller and lighter values larger. Arrows indicate current velocity where a length of  $10^\circ$  longitude equals  $1 \text{ cm s}^{-1}$ . Surface layer currents contain a strong influence of direct wind forcing while deeper currents are geostrophic.

6. Discussion

Our analyses have revealed that 400-m temperature (thermocline) anomalies have a basin-scale decadal signal which is intensified toward the western side of the North Pacific. The signal appears in both observations of upper-ocean temperature and in a model simulation forced by observed wind stresses and heat flux anomalies over the period 1970–88. Figures 1c,d show the change defined as the difference in temperature between 1980–86 and 1970–76 for both the observations and the model. Although the model thermocline response is somewhat weaker and has broader north–south extent than the observed, the basic gyre-scale structure agrees well, in spite of the uncertainties in the specified atmospheric forcing. Our model analysis demonstrates that the temperature change in the thermocline during the 1970s has a western intensified structure because of ocean dynamics. This is in contrast to the well-known pattern of SST change (e.g., Trenberth 1990; Tanimoto et al. 1993; Graham 1994; Mann and Park 1996) that occurs in the mixed layer where atmospheric surface forcing imposes spatial structures commensurate with

the atmospheric patterns which drive it (Cayan 1992; Miller et al. 1994a,b). The time variation of the deep temperature change is also more gradual than (and lags by several years) the steplike change that occurred during the 1976–77 winter in the North Pacific surface temperature, surface mixed layer depth (Polovina et al. 1994; Polovina et al. 1995; Deser et al. 1996), and other surface variables (e.g., Ebbesmeyer et al. 1991).

The model response shows that the temperature variations at depth are associated with a gyre-scale change in the upper-ocean velocity field. Figure 7 shows the gyre-scale current changes in the mixed layer, at 200 and at 400 m defined as the difference between 1980–86 and 1970–76. In the surface layer (average over the mixed layer) one sees the largest signal of velocity reflecting both the Ekman currents and the geostrophic currents. Over most of the gyre, the change weakens significantly with depth as does the mean flow (resembling an equivalent barotropic flow). The model suggests that the subpolar and subtropical gyres were strengthened by roughly 10% from the early–mid-1970s to the early–mid-1980s. This decadal-scale gyre-scale circulation adjustment<sup>1</sup> was first anticipated by Trenberth (1991), who computed the anomalous Sverdrup circulation associated with increasing midlatitude wind speeds in the 1970s, and later described by Yasuda and Hanawa (1997), who concentrated on the effect of a strengthened subtropical gyre on mode water formation (see also Qiu and Joyce 1992).

The patterns of Fig. 7 also suggest that the perturbed circulation is nearly closed by the subpolar gyre in that stronger westward flow north of 38°N feeds southward flows in the western boundary current (the Oyashio) that feeds the Kuroshio extension. This is consistent with the results of Sekine (1988) who showed the subpolar gyre theoretical Sverdrup transport increased during the periods when the Oyashio penetrated farther south. We also find an increased northward model surface-layer flow of up to 0.5 cm s<sup>-1</sup> occurs in the northeastern Pacific into the Gulf of Alaska. This is in agreement with the wind stress analysis of Lagerloef (1995), which indicates an increased Ekman flow in the gulf during that period and with the baroclinic transports calculated by Tabata (1991), which show increased geostrophic flows into the gulf over the same time interval as Fig. 7. The model however does not properly resolve the Gulf of Alaska so that the decreased strength of the Alaska gyre observed by Lagerloef (1995) from the 1970s to the 1980s in hydrographic data cannot be identified in Fig. 7.

The westward-intensified basin-scale thermocline

cooling is associated with SST cooling in the Kuroshio–Oyashio Extension, as first pointed out by Deser et al. (1996) and seen in Fig. 1 (see also Watanabe and Mizuno 1994). A model atmosphere has been shown by Peng et al. (1997) to be particularly sensitive to SST anomalies in that region. Taken together, the essential elements of midlatitude coupled ocean–atmosphere interaction (Latif and Barnett 1994; Robertson 1996) are in place in that region, namely, westward-intensified thermocline response, gyre spin up, SST signal, and atmospheric sensitivity. However, the sign of the SST signal in the Kuroshio–Oyashio Extension suggests a positive feedback rather than a negative feedback as required by the Latif–Barnett mechanism. We diagnosed the heat budget for the model mixed layer SST in the Kuroshio–Oyashio Extension region (the SST time series is shown in Fig. 1e) and found that heat-flux input dominates the decadal SST cooling (cf. Yasuda and Hanawa 1997), although water-column stability may have influenced the net effect of the heat-flux forced SST response. A higher resolution model must be used to definitively show whether gyre-scale spinup can force significant SST anomalies in the Kuroshio–Oyashio Extension. Lastly, note that the gradual SST cooling in the Kuroshio–Oyashio Extension region lags the more rapid SST cooling that occurred in the central North Pacific circa 1976–77 (Deser et al. 1996). These two SST regions may be acting independently on decadal timescales (Deser and Blackmon 1995; Nakamura et al. 1997; Zhang et al. 1997), one region being controlled mostly by gyre-scale circulation response to midlatitude wind stress curl and the other being controlled by surface heat-flux and Ekman current forcing instigated by teleconnections from the Tropics (Alexander 1992; Graham et al. 1994; Miller et al. 1994; Yukimoto et al. 1996). Decadal SST variability in the two regions may, of course, also be two manifestations of the same decadal process.

The general agreement between model Sverdrup transport changes, geostrophic velocity changes, and the change in the input observed wind stress curl over this time interval strongly supports the notion that the gyre-scale changes in circulation and thermocline are wind driven. A similar type of midlatitude decadal variation of gyre-scale circulation and upper-ocean temperature response was found by Yukimoto et al. (1996) in a coupled GCM. The interactions between variations in Pacific Ocean currents, SST, deep ocean temperature, and atmospheric variables must be better elucidated to determine if this decadal-scale variation is related to decadal-scale midlatitude Pacific ocean–atmosphere interactions found in some coupled models (e.g., Latif and Barnett 1994, 1996; Robertson 1996; Xu et al. 1998) or if it is simply a passive response of the midlatitude ocean to long timescale stochastic atmospheric forcing (Frankignoul et al. 1997; Jin 1997; James and James 1989) or teleconnected atmospheric forcing from the

<sup>1</sup> While this paper was awaiting publication, Deser et al. (1999) directly computed zonal geostrophic current changes in the Kuroshio–Oyashio Extension derived from the XBT dataset and found it consistent with Sverdrup theory based on the National Centers for Environmental Prediction reanalysis wind stress data.

Tropics (Trenberth 1990; Alexander 1992; Graham et al. 1994; Yukimoto et al. 1996).

Deser et al. (1996) additionally discovered that in the interior portion of the North Pacific a cold anomaly that was formed in the mixed layer around 1977–79 between 140° and 170°W migrated southward from 35° to 25°N and downward to 200–300-m depth along isopycnal surfaces during the ensuing 10 yr. This facet of the observed decadal temperature variations was not captured by the numerical model but it does appear in our analysis of the observations (Fig. 3, left). It is interesting to note that the westward-intensified decadal signal discussed by us here appears to be dynamically distinct from the aforementioned subducted signal of Deser et al. (1996). Thus, it is inadequate to regard thermocline variations in the North Pacific as propagating around the gyre from the Kuroshio–Oyashio to the subduction region to the southwestern subtropical gyre as suggested by Zhang and Levitus (1997) since differing physics controls the variations in different regions of the basin. The westward-intensified signals in the subpolar and subtropical gyres discussed here are driven by wind stress curl forcing, while the subducted signal is likely generated by diabatic surface processes and advected downward (Liu and Pedlosky 1994; Schneider et al. 1999). If the subducted temperature signal follows the mean isopycnals it may be salinity compensated and have no dynamical velocity anomaly associated with it or it may be a high-mode baroclinic wave associated with a velocity anomaly (Liu et al. 1998).

It is unclear why the model (constructed in isopycnal coordinates) fails to capture the subducting part of the decadal signal, though it could be due to 1) the lack of anomalous fresh-water flux forcing which could salinity compensate the temperature anomalies, 2) model mean velocities that are too weak to advect the anomaly southwards and westwards, 3) inadequate vertical resolution of isopycnal layers beneath the mixed layer or 4) a seasonal cycle of mixed layer deepening which is too regular or too deep. This latter point can be illustrated as follows. If the mixed layer cycle of deepening is irregularly influenced by very deep mixing events due to synoptic storms, then an anomalously cooled region beneath the mixed layer will have sufficient time to advect or propagate away from the source region rather than being quashed by the reappearance of the mixed layer the following winter. Additional modeling studies are needed to clarify the coupling of mixed layer processes with subducted temperature anomalies (e.g., Inui 1997; Venzke and Latif 1997; Liu 1999).

The gyre-scale change in wind stress curl forcing (Fig. 6a) results in a raised thermocline (cooler 400-m temperatures) in the western Pacific and also a deeper thermocline in the northeastern Pacific (Fig. 6c) along the California coast to the Gulf of Alaska. This may have profound influences on biological activity along the northwestern coast of North America (e.g., Brodeur et al. 1996; Mantua et al. 1997) due to a more stable

upper ocean and more reluctant upwelling of nutrients (although Schwing and Mendelssohn 1997 show summer upwelling in the California current system appears to have increased over this time period.) Although the model indicates the thermocline deepened by only 5–10 m off the western U.S. coast (Fig. 6c), it is probably underestimated as are other model variables, though it is likely to be qualitatively correct. For example, Roemmich and McGowan (1995) discuss biological productivity in the California Cooperative Oceanic Fisheries Investigations region and show it decreased after the mid-1970s at which time a warming of the upper-water column was observed. Although Miller et al. (1994) showed that surface heat fluxes were dominant in maintaining the warm SST off the California coast after 1976–77 in that region, the results here suggest the thermocline (at 180–220-m depth) was forced downward as part of a basin-scale response to wind stress curl forcing. Tropical oceanic teleconnections may also contribute to the warm upper-ocean state in the late 1970s and early 1980s (e.g., Jacobs et al. 1994; Meyers et al. 1997) but the mechanism of tropical–midlatitude communication along the eastern boundary is not yet adequately understood (e.g., Miller et al. 1997).

Because the model and observations have a similar westward-intensified response we have more confidence in these results than if we had analyzed either field in isolation. Due to sampling problems, the observations provide us with blurred images of reality due to uncertainties in both the input forcing and the output verification signal (400-m temperature). The model instead provides a dynamically consistent representation of output response to the input forcing (even though that forcing function has observational error and is therefore not the true forcing for the real ocean). The common features seen in both the model and observed output response can thus be considered real signals, which are best interpreted by a dynamical investigation of the model. Improvements in model physics, spatial resolution, and forcing functions will eventually provide a more complete understanding of the decadal signals observed in the ocean.

*Acknowledgments.* Funding was provided by NOAA under the Lamont/Scripps Consortium for Climate Research (NA47GP0188), the Scripps Experimental Climate Prediction Centre (NA36GP0372), and the Paleoclimate Program (NA66GP0274), by the National Space Development Agency of Japan, by the National Science Foundation (OCE97-11265), and by the G. Unger Vetlesen Foundation. AJM thanks Mike Alexander, Tim Barnett, Tim Baumgartner, Dave Battisti, Clara Deser, Mojib Latif, Zhengyu Liu, Sho Nakamoto, Jeff Polovina, Niklas Schneider, Frank Schwing, Yves Tourre, Kevin Trenberth, and Weimin Xu for important discussions of decadal variability.



## REFERENCES

- Alexander, M. A., 1992: Midlatitude atmosphere–ocean interaction during El Niño. 1. The North Pacific Ocean. *J. Climate*, **5**, 944–958.
- , and C. Deser, 1995: A mechanism for the recurrence of wintertime midlatitude SST anomalies. *J. Phys. Oceanogr.*, **25**, 122–137.
- Anderson, D. L. T., and A. E. Gill, 1975: Spin-up of a stratified ocean, with application to upwelling. *Deep-Sea Res.*, **22**, 583–596.
- Barsugli, J. J., and D. S. Battisti, 1998: The basic effects of atmosphere–ocean thermal coupling on midlatitude variability. *J. Atmos. Sci.*, **55**, 477–493.
- Bretherton, C. S., C. Smith, and J. M. Wallace, 1992: An intercomparison of methods for finding coupled patterns in climate data. *J. Climate*, **5**, 541–560.
- Brodeur, R. D., B. W. Frost, S. R. Hare, R. C. Francis, and W. J. Ingraham Jr., 1996: Interannual variations in zooplankton biomass in the Gulf of Alaska and covariation with California Current zooplankton biomass. *California Cooperative Oceanic Fisheries Investigations Reports*, Vol. 37, 80–99.
- Cayan, D. R., 1992: Latent and sensible heat flux anomalies over the northern oceans: Driving the sea surface temperature. *J. Phys. Oceanogr.*, **22**, 859–881.
- , A. J. Miller, T. P. Barnett, N. E. Graham, J. N. Ritchie, and J. M. Oberhuber, 1995: Seasonal–interannual fluctuations in surface temperature over the Pacific: Effects of monthly winds and heat fluxes. *Natural Climate Variability on Decadal-to-Century Time Scales*, National Academy Press, 133–150.
- Chelton, D. B., and M. G. Schlax, 1996: Global observations of oceanic Rossby waves. *Science*, **272**, 234–238.
- Deser, C., and M. Blackmon, 1995: On the relationship between tropical and North Pacific sea surface temperature variations. *J. Climate*, **8**, 1677–1680.
- , M. A. Alexander, and M. S. Timlin, 1996: Upper-ocean thermal variations in the North Pacific during 1970–1991. *J. Climate*, **9**, 1840–1855.
- , —, and —, 1999: Evidence for a wind-driven intensification of the Kuroshio Current Extension from the 1970s to the 1980s. *J. Climate*, in press.
- Ebbesmeyer, C. C., D. R. Cayan, D. R. McLain, F. H. Nichols, D. H. Peterson, and K. T. Redmond, 1991: 1976 step in the Pacific climate: Forty environmental changes between 1968–75 and 1977–1984. *Proc. 7th Ann. Pacific Climate Workshop*, Calif. Dept. of Water Resources, Interagency Ecol. Stud. Prog., Tech. Rep. 26, 115–126.
- Emery, W. J., W. G. Lee, and L. Magaard, 1984: Geographic and seasonal distributions of Brunt–Väisälä frequency and Rossby radii in the North Pacific and North Atlantic. *J. Phys. Oceanogr.*, **14**, 294–317.
- Frankignoul, C., C. Duchene, and M. A. Cane, 1989: A statistical approach to testing equatorial ocean models with observed data. *J. Phys. Oceanogr.*, **19**, 1191–1207.
- , P. Muller, and E. Zorita, 1997: A simple model of the decadal response of the ocean to stochastic wind forcing. *J. Phys. Oceanogr.*, **27**, 1533–1546.
- Graham, N. E., 1994: Decadal scale variability in the 1970s and 1980s: Observations and model results. *Climate Dyn.*, **10**, 135–162.
- , T. P. Barnett, R. Wilde, M. Ponater, and S. Schubert, 1994: Low-frequency variability in the winter circulation over the Northern Hemisphere. *J. Climate*, **7**, 1416–1442.
- Hautala, S. L., D. Roemmich, and W. L. Schmitz, 1994: Is the North Pacific in Sverdrup balance along 24°N? *J. Geophys. Res.*, **99**, 16 041–16 052.
- Inui, T., 1997: A numerical investigation of effects of westerlies variability on the circulation of subducted water. Ph.D. dissertation, Hokkaido University, Sapporo, Japan, 120 pp.
- Jacobs, G. A., H. E. Hurlburt, J. C. Kindle, E. J. Metzger, J. L. Mitchell, W. J. Teague, and A. J. Wallcraft, 1994: Decade-scale trans-Pacific propagation and warming effects of an El Niño anomaly. *Nature*, **370**, 360–363.
- James, I. N., and P. M. James, 1989: Ultra-low-frequency variability in a simple atmospheric model. *Nature*, **342**, 53–55.
- Jiang, S., F.-F. Jin, and M. Ghil, 1995: Multiple equilibria, periodic, and aperiodic solutions in a wind-driven, double-gyre, shallow-water model. *J. Phys. Oceanogr.*, **25**, 764–786.
- Jin, F.-F., 1997: A theory of interdecadal climate variability of the North Pacific ocean–atmosphere system. *J. Climate*, **10**, 1821–1835.
- Killworth, P. D., 1996: Time interpolation of forcing fields in ocean models. *J. Phys. Oceanogr.*, **26**, 136–143.
- Lagerloef, G. S. E., 1995: Interdecadal variations in the Alaska Gyre. *J. Phys. Oceanogr.*, **25**, 2242–2258.
- Latif, M., and T. P. Barnett, 1994: Causes of decadal climate variability over the North Pacific and North America. *Science*, **266**, 634–637.
- , and —, 1996: Decadal climate variability over the North Pacific and North America: Dynamics and predictability. *J. Climate*, **9**, 2407–2423.
- Levitus, S., 1982: *Climatological Atlas of the World Ocean*. NOAA Professional Paper 13, U.S. Government Printing Office, 173 pp. [Available from Superintendent of Documents, U.S. Government Printing Office, Washington, DC 20402.]
- Liu, Z., 1999: Forced planetary wave response in a thermocline gyre. *J. Phys. Oceanogr.*, in press.
- , and J. Pedlosky, 1994: Thermocline forced by annual and decadal surface temperature variation. *J. Phys. Oceanogr.*, **24**, 587–608.
- , A. Singh, S. Borisov, G. Jacobs, and R. Zhang, 1998: Planetary wave modes in thermocline circulation: Non-Doppler mode, advective mode and green mode. *Quart. J. Roy. Meteor. Soc.*, in press.
- Mann, M. E., and J. Park, 1996: Joint spatiotemporal modes of surface temperature and sea level pressure variability in the Northern Hemisphere during the last century. *J. Climate*, **9**, 2137–2162.
- Mantua, N. J., S. R. Hare, Y. Zhang, J. M. Wallace, and R. C. Francis, 1997: A Pacific interdecadal climate oscillation with impacts on salmon production. *Bull. Amer. Meteor. Soc.*, **78**, 1069–1079.
- Meyers, S. D., M. A. Johnson, M. Liu, J. J. O'Brien, and J. L. Spiesberger, 1996: Interdecadal variability in a numerical model of the northeast Pacific Ocean: 1970–89. *J. Phys. Oceanogr.*, **26**, 2635–2652.
- Miller, A. J., 1996: Recent advances in California Current modeling: Decadal and interannual thermocline variations. *California Cooperative Oceanic Fisheries Investigations Reports*, Vol. 37, 69–79.
- , D. R. Cayan, T. P. Barnett, N. E. Graham, and J. M. Oberhuber, 1994a: Interdecadal variability of the Pacific Ocean: Model response to observed heat flux and wind stress anomalies. *Climate Dyn.*, **9**, 287–302.
- , —, —, —, and —, 1994b: The 1976–77 climate shift of the Pacific Ocean. *Oceanography*, **7**, 21–26.
- , —, and J. M. Oberhuber, 1994c: On the re-emergence of midlatitude SST anomalies. *Proc. 18th Annual Climate Diagnostics Workshop*, Boulder, CO, NOAA/Climate Diagnostics Center, 149–152.
- , —, and W. B. White, 1996: Mechanisms of upper-ocean thermal variability in a 1970–88 simulation and observations. *Proc. 12th Annual PACLIM Workshop*, Pacific Grove, CA, California Department of Water Resources, 19–32.
- , W. B. White, and D. R. Cayan, 1997: North Pacific thermocline variations on ENSO timescales. *J. Phys. Oceanogr.*, **27**, 2023–2039.
- Nakamura, H., G. Lin, and T. Yamagata, 1997: Decadal climate variability in the North Pacific during recent decades. *Bull. Amer. Meteor. Soc.*, **78**, 2215–2225.
- North, G. R., T. L. Bell, R. F. Cahalan, and F. J. Moeng, 1982: Sampling errors in the estimation of empirical orthogonal functions. *Mon. Wea. Rev.*, **110**, 699–706.

- Oberhuber, J. M., 1993: Simulation of the Atlantic circulation with a coupled sea ice–mixed layer–isopycnal general circulation model. Part I: Model description. *J. Phys. Oceanogr.*, **23**, 808–829.
- Pedlosky, J., 1987: *Geophysical Fluid Dynamics*. Springer-Verlag, 710 pp.
- Peng, S., W. A. Robinson, and M. P. Hoerling, 1997: The modeled atmospheric response to midlatitude SST anomalies and its dependence on background circulation states. *J. Climate*, **10**, 971–987.
- Polovina, J., G. T. Mitchum, N. E. Graham, M. P. Craig, E. E. DeMartini, and E. N. Flint, 1994: Physical and biological consequences of a climatic event in the central North Pacific. *Fish. Oceanogr.*, **3**, 15–21.
- , —, and G. T. Evans, 1995: Decadal and basin-scale variations in mixed layer depth and the impact on biological production in the Central and North Pacific. *Deep-Sea Res.*, **42**, 1701–1716.
- Qiu, B., and T. M. Joyce, 1992: Interannual variability in the mid- and low-latitude western North Pacific. *J. Phys. Oceanogr.*, **22**, 1062–1079.
- Robertson, A. W., 1996: Interdecadal variability over the North Pacific in a multi-century climate simulation. *Climate Dyn.*, **12**, 227–241.
- , C.-C. Ma, C. R. Mechoso, and M. Ghil, 1995: Simulation of the tropical Pacific climate with a coupled ocean–atmosphere general circulation model. Part I. The seasonal cycle. *J. Climate*, **8**, 1178–1198.
- Roemmich, D., and J. McGowan, 1995: Climatic warming and the decline of zooplankton in the California Current. *Science*, **267**, 1324–1326.
- Schneider, N. S., A. J. Miller, M. A. Alexander, and C. Deser, 1999: Subduction of decadal North Pacific temperature anomalies: Observations and dynamics. *J. Phys. Oceanogr.*, in press.
- Schröter, J., and C. Wunsch, 1986: Solution of non-linear finite difference ocean models by optimization methods with sensitivity and observational strategy analysis. *J. Phys. Oceanogr.*, **16**, 1855–1874.
- Schwing, F. B., and R. Mendelssohn, 1997: Increased coastal upwelling in the California Current System. *J. Geophys. Res.*, **102**, 3421–3438.
- Sekine, Y., 1988: Anomalous southward intrusion of the Oyashio east of Japan. I. Influence of the interannual and seasonal variations in the wind stress over the North Pacific. *J. Geophys. Res.*, **93**, 2247–2255.
- Spall, M. A., 1996: Dynamics of the Gulf Stream/deep western boundary current crossover. Part II: Low-frequency internal oscillations. *J. Phys. Oceanogr.*, **26**, 2169–2182.
- Sturges, W., and B. G. Hong, 1995: Wind forcing of the Atlantic thermocline along 32°N at low frequencies. *J. Phys. Oceanogr.*, **25**, 1706–1715.
- Suga, T., and K. Hanawa, 1990: The mixed-layer climatology in the northwestern part of the North Pacific subtropical gyre and the formation area of Subtropical Mode Water. *J. Mar. Res.*, **48**, 543–566.
- Tabata, S., 1991: Annual and interannual variability of baroclinic transports across Line P in the northeast Pacific Ocean. *Deep-Sea Res.*, **38** (Suppl.), S221–S245.
- Tanimoto, Y., N. Iwasaka, K. Hanawa, and Y. Toba, 1993: Characteristic variations of sea surface temperature with multiple time scales in the North Pacific. *J. Climate*, **6**, 1153–1160.
- Tourre, Y., W. B. White, and Y. Kushnir, 1999: Evolution of interdecadal variability in SLP, SST and upper-ocean temperature over the Pacific Ocean. *J. Phys. Oceanogr.*, in press.
- Trenberth, K. E., 1990: Recent observed interdecadal climate changes in the Northern Hemisphere. *Bull. Amer. Meteor. Soc.*, **71**, 988–993.
- , 1991: Recent climate changes in the Northern Hemisphere. *Greenhouse-Gas-Induced Climatic Change: A Critical Appraisal of Simulations and Observations*, M. E. Schlesinger, Ed., Elsevier, 377–390.
- , and J. W. Hurrell, 1994: Decadal atmosphere–ocean variations in the Pacific. *Climate Dyn.*, **9**, 303–319.
- Vautard, R., and M. Ghil, 1989: Singular spectrum analysis in nonlinear dynamics with application to paleoclimatic time series. *Physica D*, **35**, 395–424.
- Venzke, S., and M. Latif, 1997: Pacific Ocean response to decadal North Pacific wind stress anomalies. *Ann. Geophys.*, **15**(Suppl.), C495.
- von Storch, H., and C. Frankignoul, 1996: Empirical modal decomposition in coastal oceanography. *The Sea, The Global Coastal Ocean*, 1–43.
- Wallace, J. M., C. Smith, and Q. Jiang, 1990: Spatial patterns of atmosphere–ocean interaction in the northern winter. *J. Climate*, **3**, 990–998.
- Watanabe, T., and K. Mizuno, 1994: Decadal changes of the thermal structure in the North Pacific. International WOCE Newsletter, No. 15, 10–13.
- Weare, B. C., and J. N. Nasstrom, 1982: Examples of extended empirical orthogonal function analyses. *Mon. Wea. Rev.*, **110**, 481–485.
- White, W. B., 1995: Design of a global observing system for gyre-scale upper ocean temperature variability. *Progress in Oceanography*, Vol. 36, Pergamon Press, 169–217.
- Xu, W., T. P. Barnett, and M. Latif, 1998: Decadal variability in the North Pacific as simulated by a hybrid coupled model. *J. Climate*, **11**, 297–312.
- Yamagata, T., and Y. Masumoto, 1992: Interdecadal natural climate variability in the Western Pacific and its implication in global warming. *J. Meteor. Soc. Japan*, **70**, 167–175.
- Yasuda, T., and K. Hanawa, 1997: Decadal changes in the mode waters in the midlatitude North Pacific. *J. Phys. Oceanogr.*, **27**, 858–870.
- Yukimoto, S., M. Endoh, Y. Kitamura, A. Kitoh, T. Motoi, A. Noda, and T. Tokioka, 1996: *Climate Dyn.*, **12**, 667–683.
- Zhang, R. H., and S. Levitus, 1997: Structure and cycle of decadal variability of upper-ocean temperature in the North Pacific. *J. Climate*, **10**, 710–727.
- Zhang, Y., J. M. Wallace, and D. S. Battisti, 1997: ENSO-like interdecadal variability: 1900–93. *J. Climate*, **10**, 1004–1020.